Global fits of SUSY at future Higgs factories

Peter Athron [2,*] Csaba Balazs [3,†] Andrew Fowlie,[2,‡] Huifang Lv,[2,§] Wei Su,[4,‖] Lei Wu [2,¶]
Jin Min Yang [5,6,**] and Yang Zhang[1,††]

[1]School of Physics, Zhengzhou University, ZhengZhou 450000, People's Republic of China
[2]Department of Physics and Institute of Theoretical Physics, Nanjing Normal University,
Nanjing 210023, People's Republic of China
[3]School of Physics and Astronomy, Monash University, Melbourne 3800 Victoria, Australia
[4]Korea Institute for Advanced Study, Seoul 02455, Korea
[5]CAS Key Laboratory of Theoretical Physics, Institute of Theoretical Physics,
Chinese Academy of Sciences, Beijing 100190, People's Republic of China
[6]School of Physics Sciences, University of Chinese Academy of Sciences,
Beijing 100049, People's Republic of China

In this work, we study the impact of electroweak and Higgs precision measurements at future electron-positron colliders on several typical supersymmetric models, including the constrained minimal supersymmetric Standard Model (CMSSM), nonuniversal Higgs mass generalizations (NUHM1, NUHM2), and the seven-dimensional minimal supersymmetric Standard Model (MSSM7). Using publicly available data from the GAMBIT community, we postprocess previous SUSY global fits with additional likelihoods to explore the discovery potential of Higgs factories, such as the Circular Electron Positron Collider (CEPC), the Future Circular Collider (FCC), and the International Linear Collider (ILC). We show that the currently allowed parameter space of these models will be further tested by future precision measurements. In particular, dark matter annihilation mechanisms may be distinguished by precise measurements of Higgs observables.

I. INTRODUCTION

After the discovery of the Higgs boson at the Large Hadron Collider (LHC), precisely measuring the properties of the Higgs boson is the next essential task for the high-energy physics community. For this purpose, various next-generation electron-positron colliders have been proposed, including the Circular Electron-Position Collider (CEPC) [1], the Compact Linear Collider (CLIC) [2], the Future Circular Collider (FCC-ee) [3], and the International Linear

*peter.athron@njnu.edu.cn
†csaba.balazs@monash.edu
‡andrew.j.fowlie@njnu.edu.cn
§lvhf@njnu.edu.cn
‖weisu@kias.re.kr
¶leiwu@njnu.edu.cn
**jmyang@itp.ac.cn
††Corresponding author.
zhangyangphy@zzu.edu.cn

Collider (ILC) [4]. These state-of-the-art machines can not only scrutinize the nature of the Higgs boson but also shed complementary light on new physics, such as low-energy supersymmetry (SUSY); for recent overviews on the status of low-energy SUSY, see e.g., [5,6]. Restricted by collision energy, these colliders may not be able to directly produce supersymmetric particles,[1] but they can provide constraints on SUSY models through high-precision measurements of the Higgs and electroweak (EW) sectors.

As is well known, global fits can provide comprehensive information on new physics models, allowing us to infer the maximum amount of information on a given model from the widest range of experimental data [9,10]. Global fits assess and compare the validity of models, identify the ranges of model parameters with the highest likelihood or posterior probability, and study the predictions and consequences for future searches. Consequently, global fits are an important part of the technical design report for future electron-positron colliders.

The GAMBIT Collaboration [11] have performed comprehensive global fits on five SUSY models; the constrained

---

[1]For some special case with rather light supersymmetric particles, see, e.g., [7,8].

minimal supersymmetric Standard Model (CMSSM) and its nonuniversal Higgs mass generalizations (NUHM1 and NUHM2) [12], the seven-dimensional weak-scale phenomenological MSSM (MSSM7) with all parameters defined at the weak scale [13], and a four-dimensional electroweakino sector of the MSSM [14]. The likelihood functions of the first four global fits include several direct and indirect dark matter (DM) searches, a large collection of electroweak precision and flavour observables, direct searches for SUSY at the Large Electron-Positron collider (LEP), and Runs I and II of the LHC, and constraints from Higgs observables. All GAMBIT input files and generated likelihood samples for these models are publicly available online through Zenodo [15,16].

As a comprehensive global fit is computationally expensive, we take full advantage of the massive sets of publicly available samples that GAMBIT generated by postprocessing them with likelihoods of expected precision limits from future electron-positron colliders. By comparing the preferred regions and best fits before and after applying such likelihoods, we can estimate the prospective reaches of future colliders. This procedure is very different from previous global fits of SUSY with future electron-positron colliders (see, e.g., [17–23]).

The paper is structured as follows. We briefly introduce the theoretical framework of the CMSSM, NUHM1, NUHM2, and MSSM7 along with their parameters in Sec. II. We then review the precision expectations of the CEPC, ILC and FCC-*ee* and present our postprocessing strategy in Sec. III. Each subsection in Sec. IV contains implications for future collider searches on the global fit of one model. Finally, we summarize the results and draw our conclusions in Sec. V.

II. THE SUPERSYMMETRIC MODELS

We restrict our consideration to specific scenarios within the *CP*-conserving, *R*-symmetric, minimal supersymmetric standard model (MSSM) [24]. The MSSM Lagrangian given in Sec. 5.4.3 of [11] defines the soft-breaking and SUSY-preserving parameters that describe the MSSM and fix our notation. Here we consider four distinct versions of the model where different constraints are applied to reduce the number of parameters.[2]

A. CMSSM

The CMSSM is the most widely studied subspace of the general MSSM [25]. It is inspired by scenarios where SUSY breaking is transmitted through supergravity interactions, fixing the soft mass parameters at very high-energy scales close to the Planck scale. Specifically, influenced by

---

[2]In all four of these models we assume that all soft-breaking parameters are real, that the explicit *CP*-violating M_1', M_2', M_3' are set to zero and that all elements of the matrices $\mathbf{C}_u$, $\mathbf{C}_d$, $\mathbf{C}_e$ vanish.

a minimal form of supergravity where the universal couplings are assumed, the universal scalar mass m_0, the gaugino mass $m_{1/2}$, and the soft-scalar trilinear A_0 masses are defined at the Grand Unified Theory (GUT) scale, M_X, through the following constraints,

$$(\mathbf{m}_F^2)_{ij}(M_X) = m_0^2 \delta_{ij}, \quad \text{for } F \in \{Q, u, d, L, e\}, \quad (1)$$

$$m_\phi^2(M_X) = m_0^2, \quad \text{for } \phi \in \{H_u, H_d\}, \quad (2)$$

$$M_i(M_X) = m_{1/2}, \quad \text{for } i \in \{1, 2, 3\}, \quad (3)$$

$$(\mathbf{A}_f)_{ij}(M_X) = \delta_{ij} A_0, \quad \text{for } f \in \{u, d, e\}. \quad (4)$$

The Yukawa and gauge couplings of the MSSM can be fixed from data, while the Higgs sector parameters μ and b (often written as m_3^2 or $B\mu$) are partially constrained by the EW vacuum expectation value (VEV), leaving the sign of the superpotential μ parameter and the ratio of the vacuum expectation values of the two Higgs doublets,

$$\tan\beta = v_u/v_d, \quad (5)$$

as free parameters. In our work we input $\tan\beta$ at the scale m_Z, following common conventions used in spectrum generators. This gives us four free continuous parameters and one free sign to fully specify scenarios in the CMSSM,

$$\text{CMSSM} : \{m_0, m_{1/2}, A_0, \tan\beta(m_Z), \text{sign}(\mu)\}. \quad (6)$$

B. NUHM1

In this variant, the supergravity inspiration of the CMSSM is maintained but the strong assumption of minimality is relaxed a little. Specifically the GUT-scale constraint on the soft scalar Higgs masses is relaxed, introducing a new free parameter m_H [26–30]. The constraint in Eq. (2) is replaced by

$$m_\phi^2(M_X) = m_H^2 \quad \text{for } \phi \in \{H_u, H_d\} \quad (7)$$

The constraints in Eqs. (1), (3), and (4) are still applied in the NUHM1. This means the predictions of the NUHM1 are determined from five free continuous parameters and one sign,

$$\text{NUHM1} : \{m_H, m_0, m_{1/2}, A_0, \tan\beta(m_Z), \text{sign}(\mu)\}. \quad (8)$$

C. NUHM2

Extending this idea slightly further, in the NUHM2 the constraint on the soft Higgs masses is even further relaxed so that $m_{H_u}(M_X)$ and $m_{H_d}(M_X)$ become independent, real, dimension-one parameters at the GUT scale. Therefore, in

the NUHM2 only the constraints in Eqs. (1), (3), and (4) are applied. This leaves six free continuous parameters and one sign to specify the physics predictions of the model,

$$\text{NUHM2} : \{m_{H_u}(M_X), m_{H_d}(M_X), m_0, m_{1/2}, A_0,$$
$$\tan\beta(m_Z), \text{sign}(\mu)\}. \quad (9)$$

D. MSSM7

In the MSSM7 the constraints are no longer applied at the GUT scale, allowing input parameters to be specified close to the weak scale and thus no longer requiring renormalization group (RG) running between this scale and the Planck scale to determine the models' physical predictions [31]. The number of parameters is reduced through the following constraints

$$(\mathbf{m}_F^2)_{ij}(Q) = m_{\tilde{f}}^2 \delta_{ij}, \quad \text{for } F \in \{Q, u, d, L, e\}, \quad (10)$$

$$M_1(Q) = \frac{\sin^2\theta_W}{3/5\cos^2\theta_W} M_2, \quad (11)$$

$$M_3(Q) = \frac{\sin^2\theta_W \alpha_s}{\alpha} M_2, \quad (12)$$

$$(\mathbf{A}_f)_{ij}(Q) = 0 \quad \forall \ (i,j) \neq (3,3), \ \text{for } f \in \{u,d\}, \quad (13)$$

$$\mathbf{A}_e(Q) = 0, \quad (14)$$

where for the weak mixing angle we use a fixed value of $\sin^2\theta_W = \frac{1}{2} - \sqrt{\frac{1}{4} - \pi\alpha/(\sqrt{2}m_Z^2 G_F)}$, which is independent of precise extractions of the gauge couplings carried out during spectrum generation. Although in principle the scale Q can be arbitrary, Eqs. (11) and (12) are inspired by the impact of the GUT relation in Eq. (3) on the gaugino masses at the weak scale. So it does not make much practical sense to choose Q too far away from this scale, and in [32] and here we fix $Q = 1$ TeV. For the sfermion sector, we assume a common sfermion mass at 1 TeV with no flavour changing and assume only the third generation up-type and down-type soft trilinear contribute non-negligibly. In the MSSM7 we also make the trade between VEVs and $|\mu|$, b. As in the NUHM2 both soft Higgs masses are free inputs, $m_{H_u}(Q)$ and $m_{H_d}(Q)$, albeit with the parameters input at very different scales which will substantially change the prior distributions they are drawn from. Similarly the sfermion masses are also no longer split by the RG flow, and the soft trilinears are treated differently with A_t and A_b as free parameters and $A_\tau = 0$. The final list of free parameters then has seven continuous parameters and one sign,

$$\text{MSSM7} : \{M_2(Q), A_{u_3}(Q), A_{d_3}(Q), m_{\tilde{f}}^2(Q), m_{H_u}^2(Q),$$
$$m_{H_d}^2(Q), \tan\beta(m_Z), \text{sign}(\mu)\}. \quad (15)$$

Global fits of these four models have previously been performed with GAMBIT in [12,13]. Here we will postprocess the results from these global fits to explore the impact of future electron-positron colliders. For the samples we use, the constraints listed above have been applied in FlexibleSUSY [32,33], which calculates the pole masses and $\overline{\text{DR}}$ couplings used in the global fit. The values of the parameters at different scales are connected by two-loop RGEs which FlexibleSUSY obtains[3] with the help of SARAH [36–39]. The scanned parameter ranges can be found in [12,13]. All dimensionful parameters are allowed to vary up to 10 TeV, safely covering scenarios that are motivated by the hierarchy problem and the most phenomenologically interesting regions within reach of colliders.

III. STUDY STRATEGY

In our analysis, we postprocess the publicly available data on Zenodo for global fits of the GUT scale SUSY models [15], and MSSM7 [16], with additional likelihoods for precision measurements of the SM Higgs observables at the proposed Higgs factories. The total likelihood is thus,

$$\mathcal{L} = \mathcal{L}_{\text{GAMBIT}} \cdot \mathcal{L}_{\text{Higgs factories}}, \quad (16)$$

where the likelihood already computed in the publicly available data, $\mathcal{L}_{\text{GAMBIT}}$, includes contributions from a large collection of present constraints on dark matter, electroweak precision, flavor observables, sparticles and the SM-like Higgs boson. Some of the constraints have been improved since the publication of the data, but they will not qualitatively affect our calculation here. Since we postprocess the data, the parameter ranges and priors are the same as in the original studies [12,13].

A Higgs factory with e^+e^- collisions at a center-of-mass energy of 240 GeV–250 GeV exploits the Higgsstrahlung process

$$e^+e^- \to hZ. \quad (17)$$

With millions of Higgs bosons produced and the clean experimental conditions at lepton colliders, both the inclusive cross section σ_{hZ} independent of the Higgs decays, and the exclusive channels of individual Higgs decays in terms of $\sigma_{hZ} \times \text{Br}$, can be measured to impressive precision. The cross sections of vector boson fusion processes for the Higgs production are relatively small at low values of center-of-mass energy. Only the main decay modes can be measured. With the center-of-mass energy increasing, the

---

[3]FlexibleSUSY also uses some code pieces from SOFTSUSY [34,35].

TABLE I. Estimated statistical precision for Higgs measurements at the proposed ILC program with various center-of-mass energies [40], the FCC-ee program with 5 ab^{-1} integrated luminosity at $\sqrt{s} = 240$ GeV and 1.5 ab^{-1} integrated luminosity at $\sqrt{s} = 365$ GeV [41,42], and the CEPC program with 20 ab^{-1} integrated luminosity at $\sqrt{s} = 240$ GeV and 1 ab^{-1} integrated luminosity at $\sqrt{s} = 360$ GeV [43].

	ILC 250 GeV 2 ab^{-1}	ILC 350 GeV 200 fb^{-1}		ILC 500 GeV 4 ab^{-1}		FCC-*ee* 240 GeV 5 ab^{-1}	FCC-*ee* 365 GeV 1.5 ab^{-1}		CEPC 240 GeV 20 ab^{-1}	CEPC 360 GeV 1 ab^{-1}	
σ_{Zh}	0.71%	2.0%		1.05%		0.5%	0.9%		0.26%	1.4%	
Decay mode	σ_{Zh} Br	σ_{Zh} Br	$\sigma_{\nu\bar{\nu}h}$ Br	σ_{Zh} Br	$\sigma_{\nu\bar{\nu}h}$ Br	σ_{Zh} Br	σ_{Zh} Br	$\sigma_{\nu\bar{\nu}h}$ Br	σ_{Zh} Br	σ_{Zh} Br	$\sigma_{\nu\bar{\nu}h}$ Br
$h \to b\bar{b}$	0.46%	1.7%	2.0%	0.63%	0.23%	0.3%	0.5%	0.9%	0.14%	0.9%	1.1%
$h \to c\bar{c}$	2.9%	12.3%	21.2%	4.5%	2.2%	2.2%	6.5%	10%	2.02%	8.8%	16%
$h \to gg$	2.5%	9.4%	8.6%	3.8%	1.5%	1.9%	3.5%	4.5%	0.81%	3.4%	4.5%
$h \to WW^*$	1.6%	6.3%	6.4%	1.9%	0.85%	1.2%	2.6%	3.0%	0.53%	2.8%	4.4%
$h \to \tau^+\tau^-$	1.1%	4.5%	17.9%	1.5%	2.5%	0.9%	1.8%	8.0%	0.42%	2.1%	4.2%
$h \to ZZ^*$	6.4%	28.0%	22.4%	8.8%	3.0%	4.4%	12%	10%	4.17%	20%	21%
$h \to \gamma\gamma$	12.0%	43.6%	50.3%	12.0%	6.8%	9.0%	18%	22%	3.02%	11%	16%
$h \to \mu^+\mu^-$	25.5%	97.3%	178.9%	30.0%	25.0%	19%	40%	...	6.36%	41%	57%
$(\nu\bar{\nu})h \to b\bar{b}$	3.7%	...	...	...	...	3.1%	...	...	1.58%	...	...

cross sections of vector boson fusion processes grow logarithmically and can provide crucial complementary information.

In Table I, we list the anticipated precision of measurements of the Higgs boson rates in the running scenarios of various machines in terms of their center of mass energies and the corresponding integrated luminosities. For the center-of-mass energy of 240 GeV–250 GeV, only the measurement of $h \to b\bar{b}$ is provided in the vector boson fusion process, which is listed in the last row.

We define the new likelihoods for the proposed Higgs factories simply as

$$-2\ln\mathcal{L}_{\text{Higgs factories}}$$
$$= \frac{(m_h - m_h^{\text{obs}})^2}{\sigma_{\mu_h}^2} + \frac{(\sigma_{Zh} - \sigma_{Zh}^{\text{obs}})^2}{\sigma_{\sigma_{Zh}}^2} + \sum \frac{(\mu_i - \mu_i^{\text{obs}})^2}{\sigma_{\mu_i}^2}, \quad (18)$$

where

$$\mu_i = \frac{\sigma_i \times \text{Br}_i}{\sigma_i^{\text{SM}} \times \text{Br}_i^{\text{SM}}}, \quad (19)$$

and the index i runs over all the Higgs search channels in Table I. We take the values of branching ratios for the 125 GeV SM Higgs as Br_i^{SM}, listed in Table II.

The total uncertainties σ_{m_h} and σ_{μ_i} consist of experimental uncertainties and theoretical uncertainties, $\sigma_{\text{tot}} = \sqrt{\sigma_{\text{the}}^2 + \sigma_{\text{exp}}^2}$. The parametric uncertainties are involved in through nuisance input parameters. For the SM Higgs mass, the present experimental uncertainty, $\sigma_{m_h}^{\text{exp}} = 0.17$ GeV [45], is already small and can be neglected compared with the theoretical uncertainty in GAMBIT, $\sigma_{m_h}^{\text{the}} = 2$ GeV. Thus, we ignore the contribution

from the Higgs mass measurement at future Higgs factories to avoid double counting the likelihood for the Higgs mass. We use the anticipated precisions displayed in Table I as the experimental uncertainties on future signal strength measurements, while the theoretical uncertainty is in the same order and therefore cannot be ignored. In Table II, we show the present theoretical uncertainties of branching ratios for the 125 GeV SM Higgs boson, which are expected to be improved in the future. We consider theoretical uncertainties $\sigma_{\mu_i}^{\text{the}} = k\sigma_{\mu_i}^{\text{SM}}$ for BSM predictions and by default we use $k = 0.2$ in our likelihood, representing a scenario where the theoretical uncertainties are reduced to the same level as the expected experimental uncertainties. However, the uncertainties on the branching ratios computed for BSM models in GAMBIT, which use SUSY−HIT1.5 [46–48] via DecayBit [49], are obviously larger than those in the SM, as carefully shown in [50] and discussed in [23]. We discuss the impacts of SUSY contributions to the uncertainties, and using different choices of k in Sec. IV B.

TABLE II. SM predictions of the decay branching ratios for the 125 GeV Higgs boson [44], as well as the relative theoretical uncertainties.

Decay mode	Branching ratio	Theoretical error
$h \to b\bar{b}$	57.7%	3.3%
$h \to c\bar{c}$	2.91%	12%
$h \to gg$	8.57%	10%
$h \to WW^*$	21.5%	4.3%
$h \to ZZ^*$	2.64%	4.3%
$h \to \gamma\gamma$	2.28×10^{-3}	5%
$h \to \tau^+\tau^-$	6.32%	5.7%
$h \to \mu^+\mu^-$	2.19×10^{-4}	6.0%

As for the central values of future signal strength measurements, μ_i^{obs}, in our scenario we assume that signal strengths predicted by the best-fit points in the GAMBIT datasets are measured. Since the GAMBIT data are sampled with Diver [51] and MultiNest [52,53], the regions around the best-fit points are densely sampled, such that our postprocessing procedure should be reasonable. Since the best-fit point agrees exactly with our assumed measurements, the best-fit point should not change through postprocessing. The extent to which the confidence regions around the best-fit shrink, however, will reveal the potential impact of precise Higgs factory measurements. We will also use other central values to check the validity of conclusions drawn from this choice in Sec. IV A.

The proposed electron-positron colliders are also designed to run at the Z pole, and have an excellent capability for precise measurements of EW observables. These measurements are complementary to the Higgs boson coupling measurements. For instance, in the so-called "blind spot" the coupling between the lightest stop and the light Higgs boson vanishes, but the stop contribution to the EW precision observables can be visible [19]. In the existing GAMBIT data, the strong coupling at the scale m_Z in the $\overline{\text{MS}}$ scheme $\alpha_s^{\overline{\text{MS}}}(m_Z)$ and the top pole mass m_t are nuisance parameters varying within $\pm 3\sigma$ of their observed central values, while the Z pole mass is fixed to 91.1876 GeV. Beside, the W mass and $\sin^2\theta_W$ are outputs calculated in PrecisionBit [49]. Therefore, we also investigate the impact of the expected EW precision measurements using

$$-2\ln\mathcal{L}_{Z\,\text{factories}} = \frac{(m_t - m_t^{\text{obs}})^2}{\sigma_{m_t}^2} + \frac{(\alpha_s^{\overline{\text{MS}}}(m_Z) - \alpha_s^{\overline{\text{MS}}}(m_Z)^{\text{obs}})^2}{\sigma_{\alpha_s^{\overline{\text{MS}}}(m_Z)}^2}$$
$$+ \frac{(m_W - m_W^{\text{obs}})^2}{\sigma_{m_W}^2} + \frac{(\sin^2\theta_W - \sin^2\theta_W^{\text{obs}})^2}{\sigma_{\sin^2\theta_W}^2}.$$

(20)

For the same reason as the $\mathcal{L}_{\text{Higgs factories}}$, we set the central values of these measurements to those predicted by the BF

point. They are listed for the CMSSM in Table III, along with the central values used in the likelihood of previous GAMBIT fits and the anticipated precisions of measurements of the EW observables at future lepton colliders. As for theoretical uncertainties, we adopt 1.5×10^{-5} for $\sin^2\theta_W$ and 1 MeV for m_W.

In total, we postprocessed 7.1×10^7 viable samples for the CMSSM, 9.4×10^7 samples for the NUHM1, 1.2×10^8 samples for the NUHM2, and 1.8×10^8 samples for the MSSM7. For each of the models the postprocessing took several days on 1280 supercomputer cores. In order to compare our results with those shown in previous GAMBIT papers [12,13], we present and plot our results in the same way. The samples are sorted into 60 bins across the range of data values in each dimension, and the resulting profile likelihoods are interpolated with a bilinear scheme in Pippi2.0 [59].

The postprocessing is performed using GAMBIT2.1.1, while the original global fits employed GAMBIT1.0. The spectrum generators in the two versions are slightly different, as GAMBIT2.1.1 includes bug fixes in calculations of the Higgs branching ratios. Therefore, the branching ratios of the SM-like Higgs in the two results are not fully consistent. Fortunately, the difference is slight and can be neglected compared to the current precision of Higgs measurements at the LHC. Using the new branching ratios, the best-fit regions in the old studies will not change qualitatively. Thus, it is still reasonable to use the results shown in papers [12,13] as the global fits of the present likelihood.

IV. RESULTS

In this section we compare profile likelihoods with and without the additional likelihood for the Higgs measurements at future electron-positron colliders, by taking CEPC as an example, in the CMSSM, NUHM1, NUHM2, and MSSM7. Moreover, the dependence of the results on assumptions about central values of Higgs measurements at future facilities and theoretical uncertainties are investigated. We also compare the sensitivities of the CEPC, FCC-ee, and ILC.

TABLE III. The theoretical predictions of EW observables for the best-fit point of CMSSM and the corresponding central values used in the previous GAMBIT fits, along with estimated statistical precisions for EW measurements at the proposed ILC, FCC-ee, and CEPC programs. The precisions are summarized in [54], which are originally from [55–58].

	CMSSM BF point	Present central value	ILC	Precision FCC-ee	CEPC
m_Z	91.1876 GeV	91.1876 GeV	2.1 MeV	0.1 MeV	0.5 MeV
m_t	173.267 GeV	173.34 GeV	0.03 GeV	0.6 GeV	0.6 GeV
$\alpha_s^{\overline{\text{MS}}}(m_Z)$	0.11862	0.1185	1.0×10^{-4}	1.0×10^{-4}	1.0×10^{-4}
m_W	80.3786 GeV	80.385 GeV	5 MeV	8 MeV	3 MeV
$\sin^2\theta_W$	0.231424	0.23155	1.3×10^{-5}	0.3×10^{-5}	4.6×10^{-5}
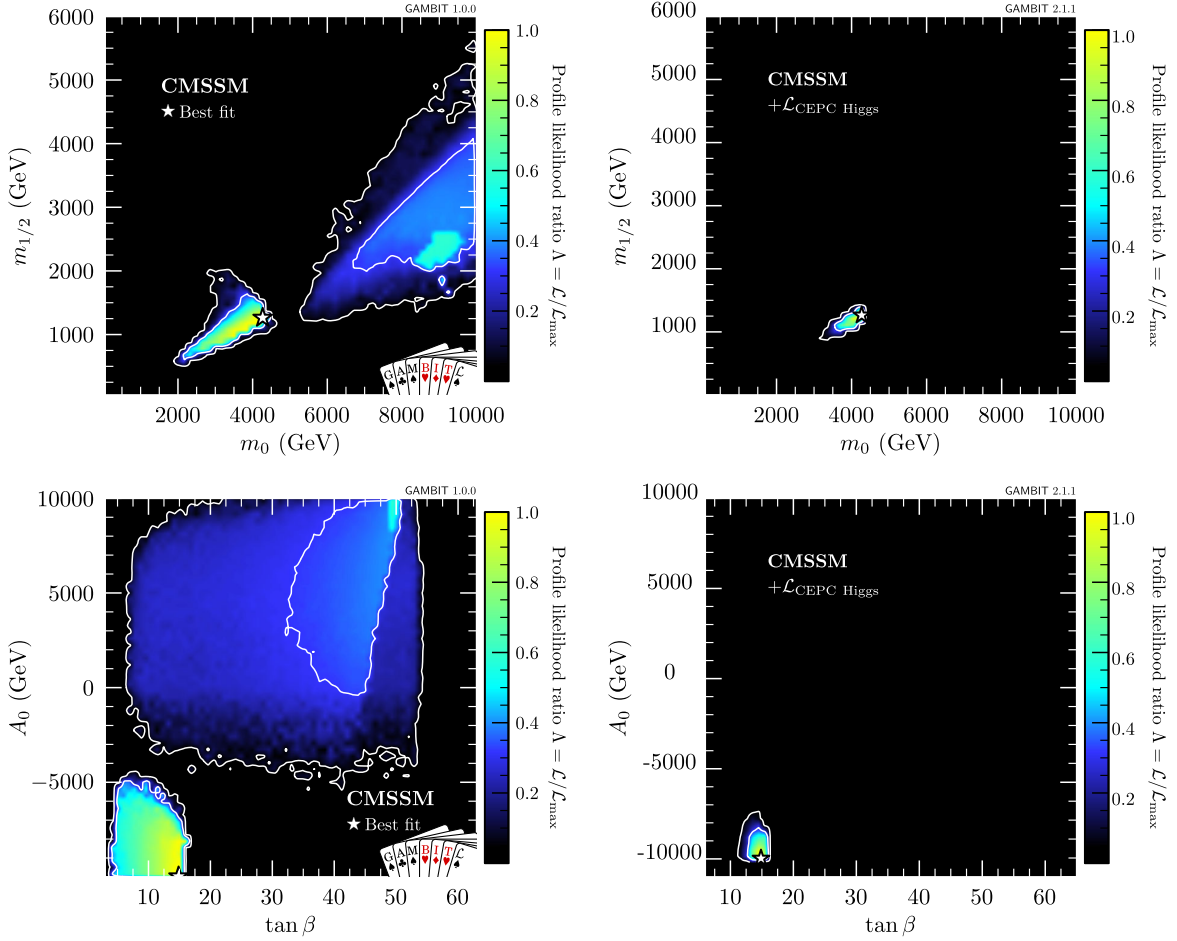
FIG. 1.   The profile likelihood ratio in the CMSSM for the present constraints (left panels, taken from [12]) and including additional CEPC measurements (right panels), with 68% and 95% C.L. contours drawn in white, and the best-fit point indicated by a star. We use the branching ratios of the best-fit point in the CMSSM as the central values of the measurements at the CEPC, and the theoretical uncertainties are $k = 0.2$ times smaller than the current SM Higgs theoretical uncertainties.

A. CMSSM

We show the 2D profile likelihoods in Fig. 1 for the input parameters of the CMSSM without (left panels) and with (right panel) the additional likelihood for the Higgs coupling measurements at the CEPC. Here we assume that the central values of measurements at the CEPC are same as those predicted by the best-fit point of the CMSSM, and the theoretical uncertainties are $k = 0.2$ times smaller than the current SM Higgs theoretical uncertainties.

We see that a large part of the region favored by present constraints is excluded by the Higgs precision measurements at the CEPC. As we use the best-fit point (the white star in the plots) to set the central values of the measurements at the CEPC, it leads to $-2 \ln \mathcal{L}_{\mathrm{CEPC}} = 0$ at the best-fit point, so the position of the best-fit point holds still, and the preferred regions shrink significantly towards the best-fit point. It is very useful to classify the regions according to the possible DM annihilation mechanisms as follows:

(i)   stop coannihilation: $m_{\tilde{t}_1} \leq 1.2 m_{\tilde{\chi}_1^0}$,
(ii) A/H-funnel: $1.6 m_{\tilde{\chi}_1^0} \leq m_{\mathrm{heavy}} \leq 2.4 m_{\tilde{\chi}_1^0}$,

(iii) chargino coannihilation: $\tilde{\chi}_1^0 \geq 50\%$ Higgsino,

where 'heavy' means a heavy Higgs-like A^0 or H^0. The best-fit point is located in the stop coannihilation region. The stop coannihilation region prefers large and negative A_0, and extends below the lower bound of bottom panels of Fig. 1. However, vacuum stability problem need to be examined carefully in this region. We see that the regions of large m_0, $m_{1/2}$, and $\tan \beta$, i.e., the A/H-funnel and chargino coannihilation regions vanish. Besides, the sign of μ in the remaining stop coannihilation regions is always negative.

The sign of the μ parameter highly affects several physical observables, such as the recently updated anomalous magnetic moment of the muon a_μ [60]. As mentioned in [12], the fit favors $\mu < 0$ versus $\mu > 0$ by $\Delta \ln \mathcal{L} = 0.4$, mainly because of the LHC Higgs signal likelihood. With the impressive precision of Higgs property measurements at the CEPC, the distinction between $\mu > 0$ and $\mu < 0$ reaches more than 2σ.

Note that the classification of dark matter annihilation mechanisms is not exclusive. A sample can lie in more than

one region. The classifications provide information about the relationship between sparticle masses. Samples in the same region have similar parameter values and mass spectra, as well as similar SM Higgs branching ratios.

In order to further understand the significant impact of the CEPC, as shown in Fig. 1, we display the SM-like Higgs decay branching ratios predicted by the best-fit points in each of the regions in Table IV. The combined experimental and theoretical uncertainty is also shown. The parameter values, mass spectra, and present likelihood contributions of these best-fit points can be found in [12]. We see that the differences in $\mathrm{BR}(h \to b\bar{b})$, $\mathrm{BR}(h \to WW^*)$ and $\mathrm{BR}(h \to ZZ^*)$ between the best-fit points of the stop coannihilation region and the A/H-funnel region or the $\tilde{\chi}_1^\pm$ coannihilation regions are significantly larger than the corresponding total uncertainties. This is the reason why the A/H-funnel region and the $\tilde{\chi}_1^\pm$ coannihilation region are excluded when we assume that the CEPC measures exactly the central values predicted by the best-fit point in the stop coannihilation region.

It is obvious that the results shown in Fig. 1 and the above conclusions depend on assumptions about central values of the Higgs measurements at the CEPC. Therefore, in Fig. 2 we display the 2D profile likelihoods assuming the central values of the Higgs measurements at the CEPC to be the values of the best-fit point in each DM annihilation region, not just the overall best-fit point. Whereas the A/H-funnel region predicts SM-like Higgs couplings, the $\tilde{\chi}_1^\pm$ and

TABLE IV. SM-like Higgs signal strengths and normalized cross sections of the best-fit points for the present likelihood in the CMSSM, for each of the regions characterized by a specific mechanism for suppressing the relic density of dark matter. We also give the total uncertainty used in $\mathcal{L}_{\mathrm{CEPC}}$ in the last column, assuming $k = 0.2$.

	A/H-funnel	$\tilde{\chi}_1^\pm$ coannihilation	$\tilde{t}$ coannihilation	
A_0	9924.435	9206.079	−9965.036	
m_0	9136.379	9000.628	4269.402	
$m_{1/2}$	2532.163	2256.472	1266.043	
$\tan\beta$	49.048	49.879	14.857	
$\mathrm{sgn}(\mu)$	...	...	...	Total error
$\sigma_{Zh}/\sigma_{Zh}^{\mathrm{SM}}$	0.975	0.977	0.975	0.5%
$\mu_{(Z)h \to b\bar{b}}$	1.018	1.031	0.995	0.71%
$\mu_{(Z)h \to c\bar{c}}$	1.135	1.125	1.154	4.08%
$\mu_{(Z)h \to gg}$	0.775	0.768	0.745	2.38%
$\mu_{(Z)h \to WW^*}$	0.913	0.900	0.974	1.31%
$\mu_{(Z)h \to ZZ^*}$	0.934	0.919	1.003	5.17%
$\mu_{(Z)h \to \gamma\gamma}$	1.127	1.116	1.182	6.87%
$\mu_{(Z)h \to \tau^+\tau^-}$	0.983	0.978	0.994	1.39%
$\mu_{(Z)h \to \mu^+\mu^-}$	1.004	0.999	1.015	17.04%
$\mu_{(\nu\bar{\nu})h \to \mu^+\mu^-}$	0.997	1.010	0.977	2.87%

stop co-annihilation predictions for the CEPC are expected to be in about 1σ and 5σ tension with the SM, respectively.

It can be seen that the favored regions change dramatically with the central values changing from the values of one best-fit point to another. As expected, the center of the favored regions is on the chosen best-fit point. In the bottom left panel of Fig. 2, where the central values are the same as the best-fit point in the A/H-funnel region, the favored regions are not as narrow as before. There is a small stop coannihilation region inside the 95% C.L. region. The samples in the 95% C.L. region of $m_0 < 8.5$ TeV and $m_{1/2} > 2.6$ TeV mainly satisfy the $\tilde{\chi}_1^\pm$ coannihilation condition, while the 68% C.L. region is almost pure A/H-funnel region. In the whole region, the μ parameter is always negative. The confidence regions found when setting the central values of the CEPC measurements to those predicted by the best-fit point in the $\tilde{\chi}_1^\pm$ coannihilation region, shown in the bottom-right panel of Fig. 2, are even wider. All three DM annihilation regions exist in the 68% C.L. region. However, there are no samples with $\mu > 0$ in the 95% C.L. region.

The sfermions in the A/H-funnel and the $\tilde{\chi}_1^\pm$ coannihilation regions are heavier than about 5 TeV. For instance, the best-fit point in the $\tilde{\chi}_1^\pm$ coannihilation region has $m_{\tilde{t}_1} \simeq m_{\tilde{\tau}_1} \simeq 6.5$ TeV and $m_{\tilde{q}} \simeq 10$ TeV for the first two generation sfermions. The supersymmetric contributions to the SM-like Higgs branching ratios tend to decouple in the high-mass region. Nevertheless, the SM-like Higgs branching ratios in these regions remain quite different from the SM values listed in Table II. Various uncertainties and factors are involved in this discrepancy, such as values of SM parameters used in the calculations. Therefore, it further inspires us not to set the central values of the Higgs measurements at future Higgs factories to the SM values listed in Table II. To some extent, the SM-like Higgs branching ratios of a point in the high mass region can be treated as the SM values, such as the best-fit point of the A/H-funnel region or the $\tilde{\chi}_1^\pm$ coannihilation region.

We also show the 2D profile likelihood for EW measurements at the CEPC in Fig. 3, where the left panel implements the EW measurements on their own and the right panel combines likelihoods for the EW and Higgs measurements. The EW measurements visibly narrow the favored regions, though not to the same degree as the Higgs measurements. The two kinds of measurements complement each other well, as combining them gives extremely strong constraints on the parameter space of the CMSSM, shown in the right panel of Fig. 3. The best-fit point's predictions for EW observables are expected to be in about 3σ tension with the SM.

B. NUHM1 and NUHM2

In the right panels of Fig. 4 we show the joint profile likelihood ratio including the proposed CEPC constraints

FIG. 2. Two-dimensional profile likelihoods for the CMSSM with an additional likelihood for CEPC, with different assumptions about the central values of Higgs measurements at the CEPC. The top left panel (taken from [12]) shows the mechanisms that ensure that the dark matter relic density does not exceed the measured value across the 2σ contours of the present likelihoods, with the best-fit point in each region indicated by a star. The rest of the panels assume the central values of the Higgs measurements at the CEPC are the values of the best-fit point in the stop coannihilation region (top right), in the A/H-funnel region (bottom left) and in the $\tilde{\chi}_1^{\pm}$ coannihilation region (bottom right).
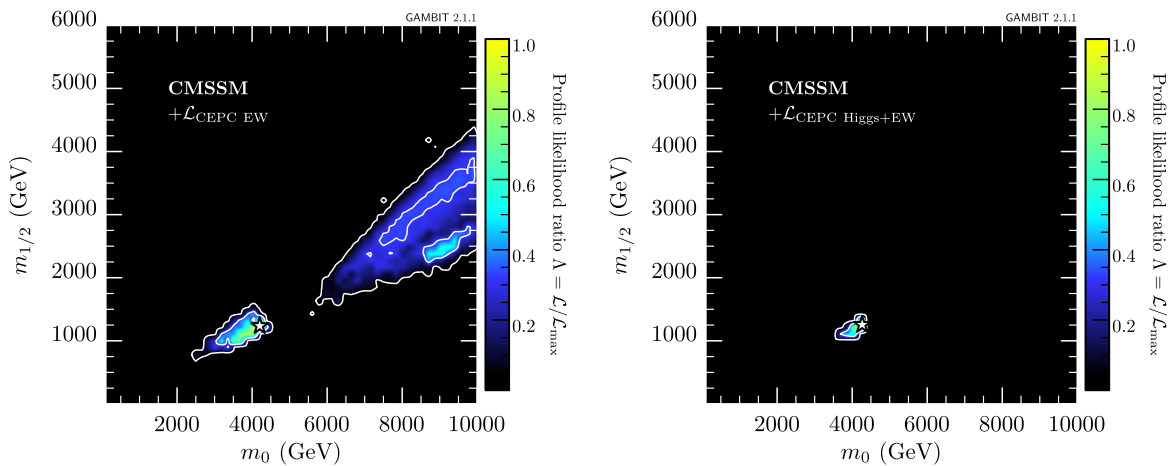
FIG. 3. 2D profile likelihoods for the CMSSM, plotted in the $m_0 - m_{1/2}$ plane, adding only likelihood of EW measurements at CEPC (left) and adding likelihoods of EW measurements and Higgs measurements at CEPC (right). The assumptions about CEPC likelihood for Higgs measurements are as Fig. 1.
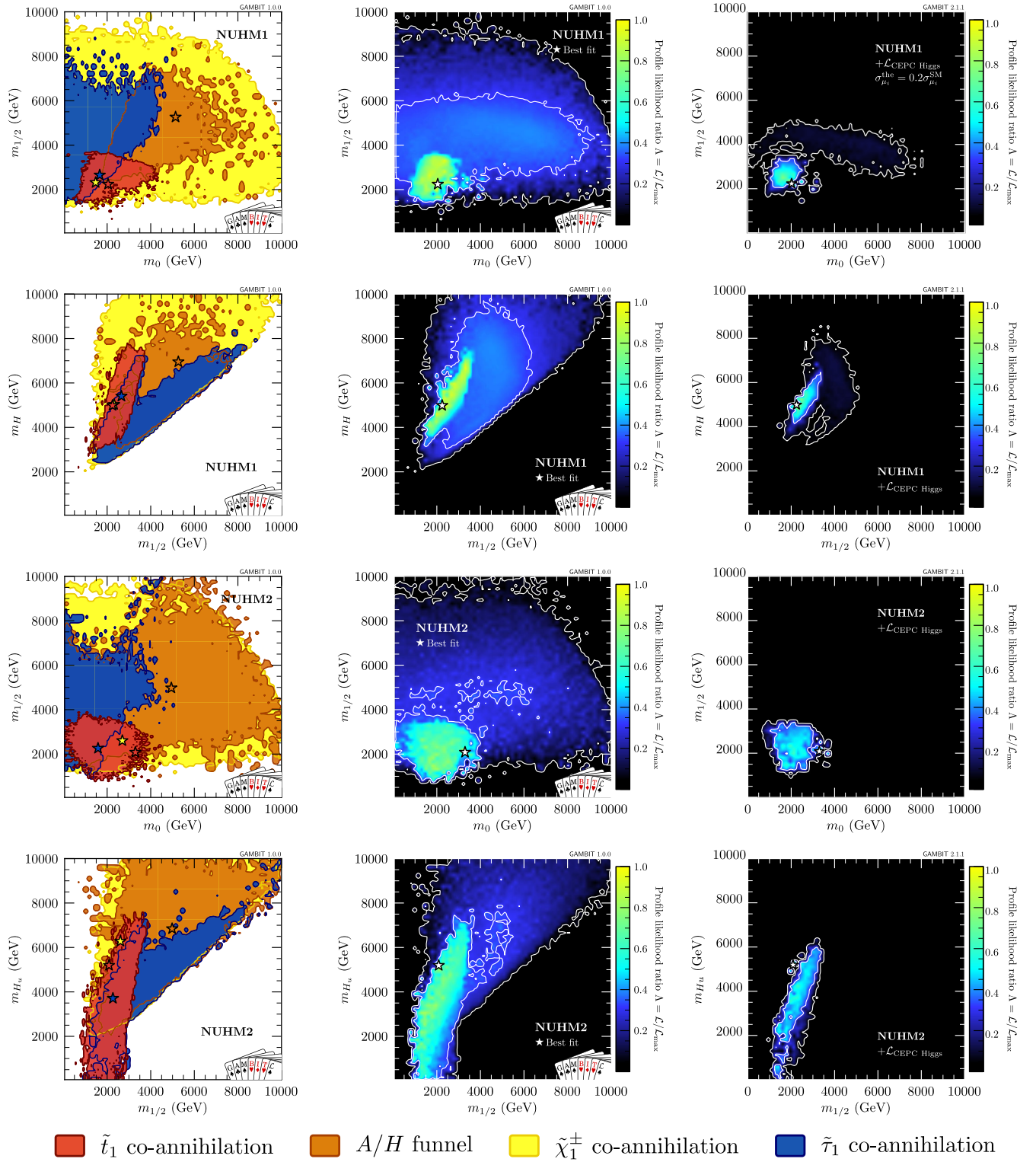
FIG. 4. Profile likelihood ratio, without the CEPC likelihood (middle panels, taken from [12]) and with the CEPC likelihood (right panels), for the NUHM1 (top two rows) and the NUHM2 (bottom two rows). Color-coding in the left panels (taken from [12]) shows the mechanisms active in models within the 95% C.L. contour for avoiding thermal overproduction of neutralino dark matter. The overall best-fit point is indicated by a white star, while the best-fit points in each region are indicated by colored stars. The assumptions about the CEPC likelihood are the same as those in Fig. 1.
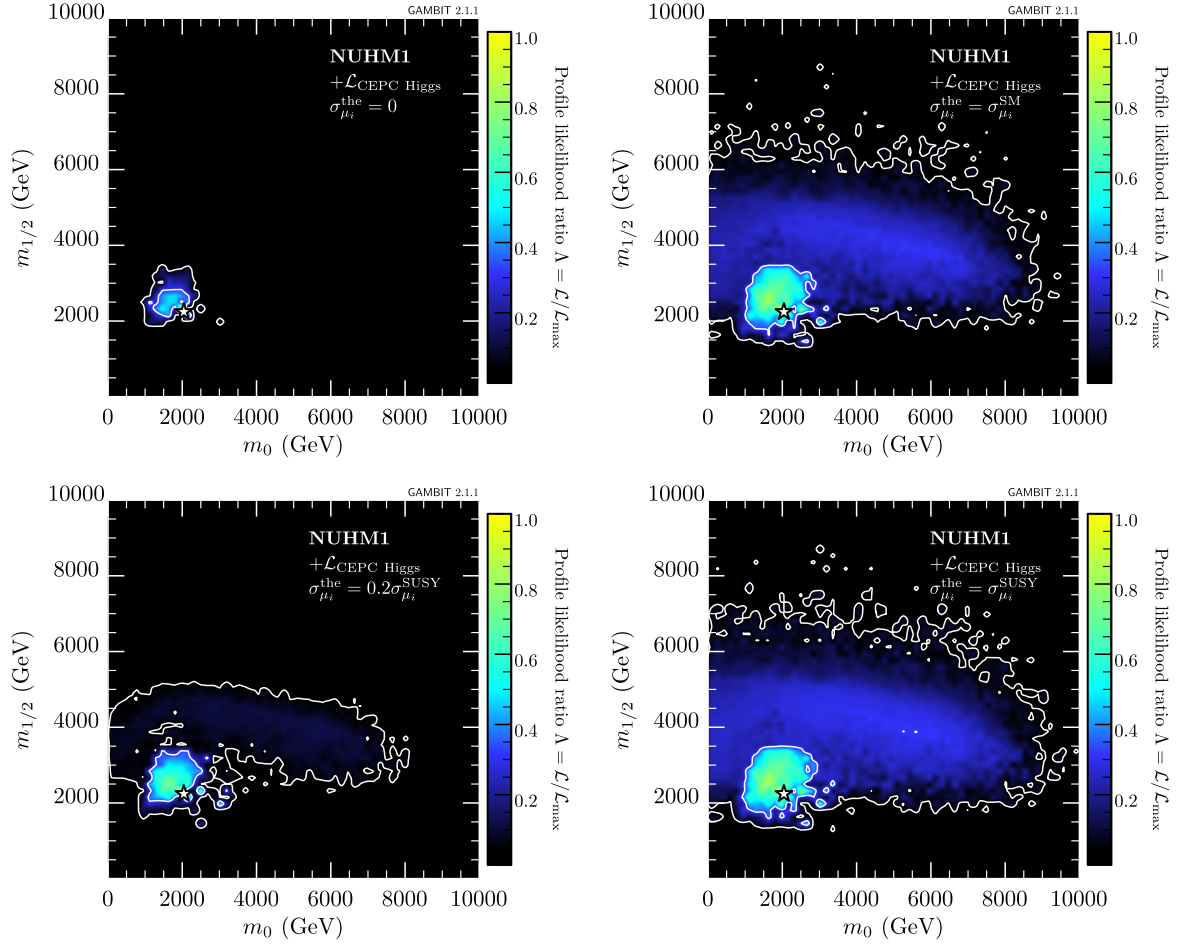
FIG. 5. Profile likelihood ratio assuming no theoretical uncertainties on the signal strength at CEPC (top left panel), assuming the future theoretical uncertainties equal to the current theoretical uncertainties of the SM Higgs (top right panel), and taking SUSY contributions to the theoretical uncertainties into consideration (bottom panels), plotted in the m_0–$m_{1/2}$ plane of the NUHM1.

for the input model parameters of the NUHM1 and NUHM2, accompanied by the profile likelihood ratio without $\mathcal{L}_{\text{CEPC}}$ in the middle panels and the dark matter annihilation mechanisms in the left panels. The definitions of the dark matter annihilation regions are same as those in the above subsection, except for an additional category

(i) *stau coannihilation:* $m_{\tilde{\tau}_1} \leq 1.2 m_{\tilde{\chi}_1^0}$,
which is absent in the CMSSM results. With the extra freedom presented in the Higgs sector of the nonuniversal Higgs mass models, the μ parameters decouple from m_0, leading to arbitrarily light Higgsinos. Thus, the chargino coannihilation region expands significantly. Meanwhile, the best-fit points in both the NUHM1 and NUHM2 results are also located in the stop co-annihilation region and have slightly larger likelihoods than the best-fit point in the CMSSM.

As in the CMSSM, with the addition of $\mathcal{L}_{\text{CEPC}}$, the preferred regions shrink significantly towards the best-fit points in the NUHM1. However, the stop coannihilation region here overlaps with all other three regions in all of the parameter planes. As a result, the remaining 2σ regions also

contain some chargino coannihilation region. Note that the 1σ region is a pure stop coannihilation region. Samples of $\mu > 0$ are all excluded. In comparison to the NUHM1 results, the NUHM2 results show larger 1σ regions but smaller 2σ regions, with no chargino coannihilation region inside the 2σ region.

The extent of the confidence regions surrounding the best-fit point depends to some degree on the assumptions made about the theoretical uncertainties on the Higgs branching ratios. Comparing with the top right panel of Fig. 4 which uses 0.2 of the current theoretical uncertainties in $\mathcal{L}_{\text{CEPC}}$, we show the result without theoretical uncertainties and with full current SM theoretical uncertainties in the top left and top right panel of Fig. 5, respectively. In general the confidence region shrinks a lot with smaller theoretical uncertainties, though the dark matter annihilation mechanisms and the sign of μ in the 1σ regions remain the same. Without theoretical uncertainties, only small regions around the best-fit point remain. Assuming no improvement on the theoretical uncertainties, the favored regions still shrink, but this would substantially negate the
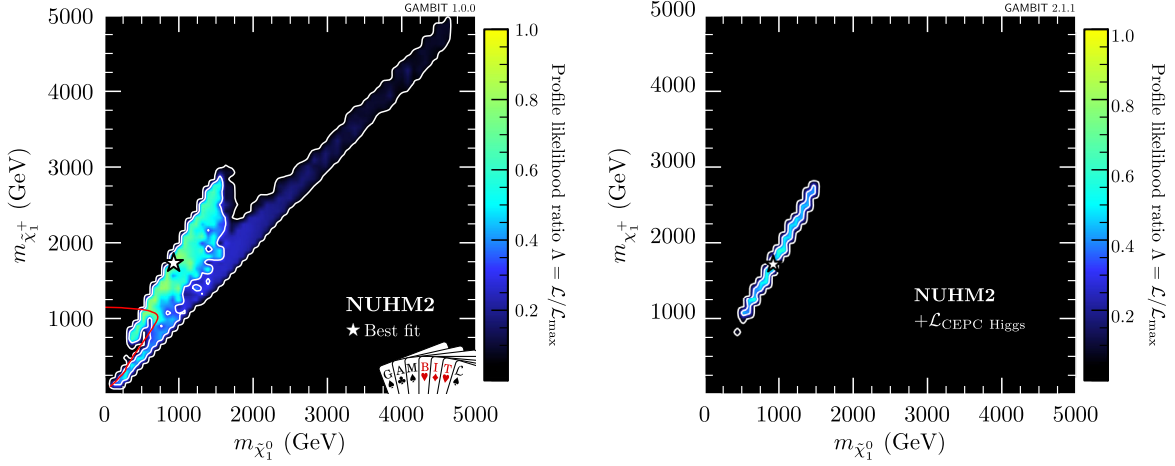
FIG. 6.   Profile likelihoods for the NUHM2 without CEPC likelihood (left panels) and with CEPC likelihood (right panels), plotted in the $\tilde{\chi}_1^{\pm} - \tilde{\chi}_1^0$ mass plane.

advantage of Higgs factories. In addition, we add SUSY contributions to the theoretical uncertainties according to Ref. [23], and display the results in bottom panels of Fig. 5. Here $\sigma_{\mu_i}^{\mathrm{SUSY}}$ are the theoretical uncertainties including SUSY contributions based on $\sigma_{\mu_i}^{\mathrm{SM}}$, namely 5% for Higgs decaying to quark pair and lepton pair, 5% for $h \to WW^*$ and ZZ^*, and 3% for $h \to \gamma\gamma$. In the bottom-left panel we show the impact if the $\sigma_{\mu_i}^{\mathrm{SUSY}}$ are reduced by a factor of 5, while in the bottom right, in contrast, we use the current uncertainties. The bottom-left panel of Fig. 5 can be compared with the top right panel of Fig. 4. They mildly enlarged the 1σ and 2σ regions, as expected. We see that assumptions about the theoretical uncertainties for the Higgs branching ratios clearly influence the global fit results when including the Higgs measurements at the CEPC, though not as much as the choice of which central values are used in the likelihood.

In Fig. 6, we show the results on the $m_{\tilde{\chi}_1^{\pm}}$–$m_{\tilde{\chi}_1^0}$ plane. We see that as the dark matter annihilation mechanisms constrain the dark matter mass and the relationships between sparticle masses, and that the masses of relevant sparticles are further restricted into limited ranges by $\mathcal{L}_{\mathrm{CEPC}}$. In the stop co-annihilation region, the wino-dominated chargino mass is about twice as large as the bino-dominated dark matter mass, because $M_1 : M_2 \simeq 1 : 2$ at the low scale produced by $M_1 = M_2$ at the GUT scale. As the chargino coannihilation regions are fully excluded, it sets upper limits of 1.7 TeV on $m_{\tilde{\chi}_1^0}$ and 3 TeV on $m_{\tilde{\chi}_1^{\pm}}$.

C. MSSM7

The results of the MSSM7 scan are shown in Fig. 7, on the parameter planes of μ–M_1, M_2–$m_{\tilde{f}}$ and μ–$\tan\beta$, and on the mass plane of $\tilde{\chi}_1^0$–$\tilde{t}_1$. Here μ and M_1 are presented at the scale $M_{\mathrm{SUSY}} = \sqrt{m_{\tilde{t}_1} m_{\tilde{t}_2}}$. Two new regions

(i) sbottom coannihilation: $m_{\tilde{b}_1} \le 1.2 m_{\tilde{\chi}_1^0}$,

(ii) h/Z funnel: $1.6 m_{\tilde{\chi}_1^0} \le m_{\mathrm{light}} \le 2.4 m_{\tilde{\chi}_1^0}$,
appear, where 'light' may be h or Z. In the sbottom coannihilation region, the lightest sfermion is $\tilde{t}_1$ and therefore it highly overlaps with the stop co-annihilation region. In contrast to the GUT-scale models, the overall best-fit point of the MSSM7 is located in the chargino coannihilation region, and the corresponding best-fit likelihood is improved.

We see that the 1σ ranges are shrunk significantly, similar to the results of GUT-scale models, but the 2σ ranges of parameters are not visibly reduced by the CEPC constraints, except for the μ parameter. With free $m_{H_u}^2$ and $m_{H_d}^2$, the lightest chargino and neutralino can be higgsino-dominated for almost any value of M_2, $m_{\tilde{f}}$, A_{d_3}, A_{u_3}, and $\tan\beta$. Considering that we set the central values of Higgs measurements at CEPC to the values of the overall best-fit point, most of the chargino coannihilation region survives. Thus, the ranges of those parameters cannot be restricted. On the other hand, the μ parameter has to be lighter than M_1 in the chargino coannihilation region, so that the lightest chargino is not bino-dominated, shown in the top left panel of Fig. 7. When the other regions are excluded, the upper limit on μ drops accordingly.

As the A/H funnel region and the chargino coannihilation region overlap heavily in all the planes, part of the A/H funnel regions escapes from the restriction of the CEPC Higgs measurements. Besides, there are a few samples satisfying the stop and sbottom coannihilation conditions, which can be seen in the low panels of Fig. 7, but they fulfill the A/H funnel selection at the same time. We also see one sample satisfying the h/Z funnel and the chargino coannihilation conditions simultaneously. Overall, Higgs measurements at the CEPC do not have much power to discriminate between different DM annihilation mechanisms in the MSSM7.
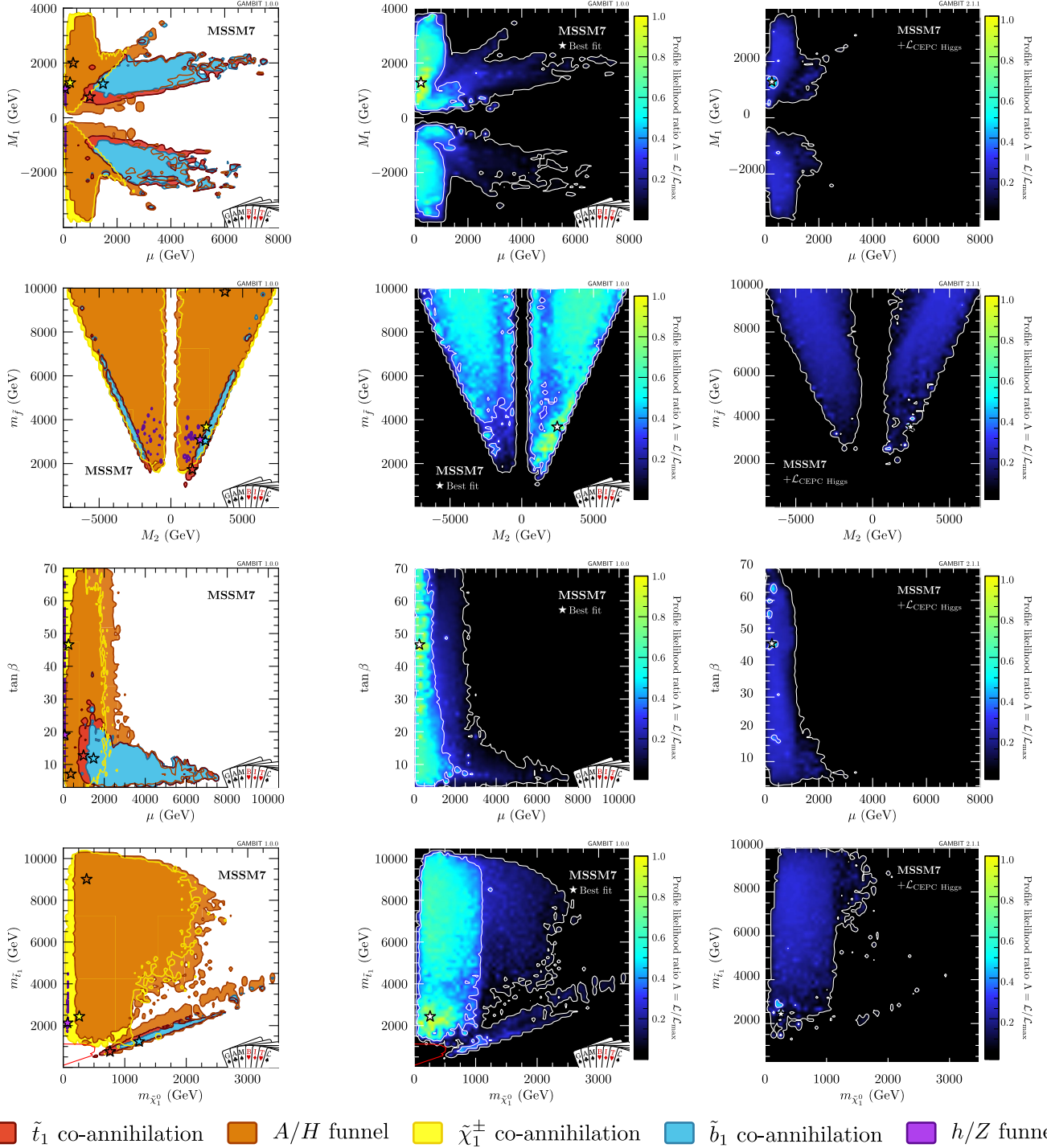
FIG. 7.   Profile likelihood ratio without the CEPC likelihood (middle panels, taken from [13]) and with the CEPC likelihood (right panels) for the MSSM7. Color coding in the left panels (taken from [13]) shows the mechanisms active in models within the 95% C.L. contour for avoiding thermal overproduction of neutralino dark matter. The overall best-fit point is indicated by a white star, while the best-fit points in each region are indicated by colored stars. The assumptions about the CEPC likelihood are the same as those in Fig. 1.

We present a brief comparison for the potential reach of the CEPC, FCC-*ee* and ILC in Fig. 8, together with the top left of Fig. 7. The results include measurements at all proposed center-of-mass energies listed in Table I. The CEPC and ILC result in slightly stronger constraints than the FCC-*ee* and almost same contour regions, but for different reasons. The CEPC proposes a higher integrated luminosity at $\sqrt{s} = 250$ GeV, while the ILC has more center of mass-energy options. The difference of favored regions between these facilities are small due to the
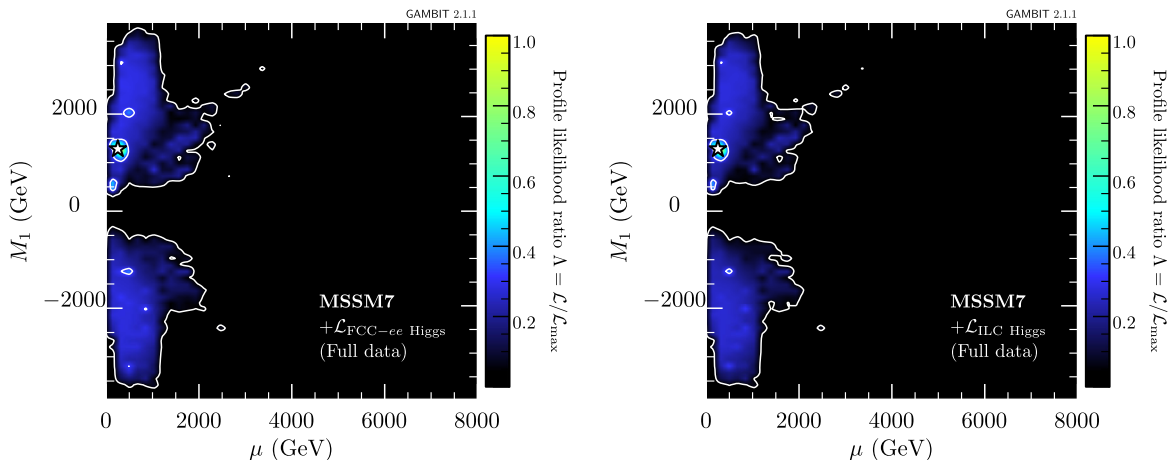
FIG. 8. Profile likelihood ratio for the MSSM7, comparison between the potential reach of FCC-*ee* and ILC.

theoretical uncertainties which are larger than the anticipated precision in some signal channels.

Before concluding, we consider the implications on our models of two outstanding experimental anomalies. First, the surviving regions shown for all of these SUSY models cannot make a significant contribution to resolving the recently updated muon $g - 2$ anomaly [60], as the unified sfermion mass $m_{\tilde{f}}$ is pushed to a relatively large value by other constraints, such as LHC sparticle searches and B-physics constraints. An MSSM explanation of the muon $g - 2$ anomaly at the 2σ level requires light EWinos and light sleptons (see, e.g., [61–64]), which may be accessible at the future runs of the LHC [64,65].

Second, the new CDF II measurement of the W-boson mass shows a 7σ deviation from the SM prediction [66]. This differs significantly from the central value used for m_W in previous GAMBIT fits. Therefore, all samples in our favored regions disagree with the new measurement by at least 2σ. In any case, it is difficult to explain the large deviation in the general MSSM [67–69].

Finally, let us remark on the issue of naturalness in our scenarios. We quantified the fine tuning for the best fit points in the GUT-scale SUSY models through

$$\Delta_\mu = \frac{\partial \ln M_Z^2}{\partial \ln \mu^2} \qquad (21)$$

Using SuSpect [70], we found about 4000 for the CMSSM, 700 for the NUHM1 and 900 for the NUHM2. The fine-tuning in the favored regions of the CMSSM is generally larger than that in the NUHM1/2, because the condition $m_0^2 = m_{H_u}^2 = m_{H_d}^2$ leads to a strict constraint on m_0. Investigating the fine-tuning cost comprehensively is beyond the scope of this paper, but the fine tuning of these benchmarks should be a reasonable indication of the typical level of tuning one expects in the surviving samples.

V. CONCLUSIONS

Utilizing the publicly available data for SUSY global fits from the GAMBIT community, we examined the potential impact of measurements at proposed Higgs factories on several constrained versions of the MSSM, namely the CMSSM, NUHM1, NUHM2, and MSSM7. We postprocessed all the samples to calculate the likelihood for Higgs measurements from the CEPC as an example, and then compared profile likelihood ratios with and without this additional likelihood from the CEPC. The preferred regions in these models are significantly shrunk by the precise Higgs measurements at the CEPC. As a result, the possible dark matter annihilation mechanisms in the models and signs of μ parameter could be distinguished by CEPC measurements. Comparing results in different models, the constraints on model parameters are weaker in models with more input parameters, i.e., looser correlations between model parameters. The specific favored and excluded parameter regions highly depends on the assumed central values of the Higgs measurements, and are mildly dependent on assumptions about theoretical uncertainties. Since the projected experimental uncertainties are even better than the current theoretical uncertainties, reaches of Higgs factories are dominated by the theoretical uncertainties. Reducing these theory uncertainties is an important and significant challenge. Under the assumption that the future theoretical uncertainties could be reduced to the same level of expected experimental uncertainties, we compared the impact of the CEPC, FCC-*ee* and ILC on the MSSM7. We found that their reaches are quite similar, and slightly better with higher proposed luminosity or higher center-of-mass energy, as expected. In summary, with high-precision Higgs coupling measurements, future Higgs factories can significantly advance our understanding of the MSSM parameter space and mass spectrum, and could be complementary to dark matter searches and EW precision measurements.

[1] M. Dong *et al.* (CEPC Study Group Collaboration), CEPC Conceptual Design Report: Volume 2—Physics & Detector, arXiv:1811.10545.

[2] T. Charles *et al.* (CLICdp, CLIC Collaboration), *The Compact Linear Collider (CLIC)—2018 Summary Report* (CERN, Geneva, 2018), Vol. 2.

[3] M. Bicer *et al.* (TLEP Design Study Working Group Collaboration), First Look at the Physics Case of TLEP, J. High Energy Phys. 01 (2014) 164.

[4] The International Linear Collider Technical Design Report —Volume 2: Physics, arXiv:1306.6352.

[5] H. Baer, V. Barger, S. Salam, D. Sengupta, and K. Sinha, Status of weak scale supersymmetry after LHC Run 2 and ton-scale noble liquid WIMP searches, Eur. Phys. J. Special Topics **229**, 3085 (2020).

[6] F. Wang, W. Wang, J. M. Yang, Y. Zhang, and B. Zhu, Low energy supersymmetry confronted with current experiments: An overview, Universe **8**, 178 (2022).

[7] J.-R. Yuan, H.-J. Cheng, and X.-A. Zhuang, Prospects for chargino pair production at the CEPC *, Chin. Phys. C **46**, 013104 (2022).

[8] J. Chen, C. Han, J. M. Yang, and M. Zhang, Probing a bino NLSP at lepton colliders, Phys. Rev. D **104**, 015009 (2021).

[9] A. Kvellestad, P. Scott, and M. White, GAMBIT and its application in the search for physics beyond the standard model, Prog. Part. Nucl. Phys. **113**, 103769 (2020).

[10] S. S. AbdusSalam *et al.*, Simple and statistically sound strategies for analysing physical theories, Rep. Prog. Phys. **85**, 052201 (2022).

[11] P. Athron *et al.* (GAMBIT Collaboration), GAMBIT: The global and modular beyond-the-standard-model inference tool, Eur. Phys. J. C **77**, 784 (2017).

[12] P. Athron *et al.* (GAMBIT Collaboration), Global fits of GUT-scale SUSY models with GAMBIT, Eur. Phys. J. C **77**, 824 (2017).

[13] P. Athron *et al.* (GAMBIT Collaboration), A global fit of the MSSM with GAMBIT, Eur. Phys. J. C **77**, 879 (2017).

[14] P. Athron *et al.* (GAMBIT Collaboration), Combined collider constraints on neutralinos and charginos, Eur. Phys. J. C **79**, 395 (2019).

[15] GAMBIT Collaboration, Supplementary Data: Global fits of GUT-scale SUSY models with GAMBIT, Eur. Phys. J. C **77**, 824 (2017).

[16] GAMBIT Collaboration, Supplementary Data: A global fit of the MSSM with GAMBIT, Eur. Phys. J. C **77**, 879 (2017).

[17] J. Ellis and T. You, Sensitivities of prospective future e^+e^- colliders to decoupled new physics, J. High Energy Phys. 03 (2016) 089.

[18] J. Fan and M. Reece, A new look at Higgs constraints on stops, J. High Energy Phys. 06 (2014) 031.

[19] J. Fan, M. Reece, and L.-T. Wang, Precision natural SUSY at CEPC, FCC-ee, and ILC, J. High Energy Phys. 08 (2015) 152.

[20] W. Su and J. M. Yang, SUSY effects in R_b: Revisited under current experimental constraints, Phys. Lett. B **757**, 136 (2016).

[21] N. Liu and L. Wu, An indirect probe of the higgsino world at the CEPC, Eur. Phys. J. C **77**, 868 (2017).

[22] H. Li, H. Song, S. Su, W. Su, and J. M. Yang, MSSM at future Higgs factories, Chin. Phys. C **45**, 045106 (2021).

[23] A. Arbey, M. Battaglia, A. Djouadi, F. Mahmoudi, M. Muhlleitner, and M. Spira, Higgs properties and supersymmetry: Constraints and sensitivity from the LHC to an e^+e^- collider, arXiv:2201.00070.

[24] P. Fayet, The supersymmetric standard model, Adv. Ser. Dir. High Energy Phys. **26**, 397 (2016).

[25] H. P. Nilles, Supersymmetry, supergravity and particle physics, Phys. Rep. **110**, 1 (1984).

[26] D. Matalliotakis and H. P. Nilles, Implications of nonuniversality of soft terms in supersymmetric grand unified theories, Nucl. Phys. **B435**, 115 (1995).

[27] M. Olechowski and S. Pokorski, Electroweak symmetry breaking with nonuniversal scalar soft terms and large tan beta solutions, Phys. Lett. B **344**, 201 (1995).

[28] V. Berezinsky, A. Bottino, J. R. Ellis, N. Fornengo, G. Mignola, and S. Scopel, Neutralino dark matter in supersymmetric models with nonuniversal scalar mass terms, Astropart. Phys. **5**, 1 (1996).

[29] M. Drees, M. M. Nojiri, D. P. Roy, and Y. Yamada, Light Higgsino dark matter, Phys. Rev. D **56**, 276 (1997).

[30] P. Nath and R. L. Arnowitt, Nonuniversal soft SUSY breaking and dark matter, Phys. Rev. D **56**, 2820 (1997).

[31] A. Djouadi *et al.* (MSSM Working Group Collaboration), The Minimal supersymmetric standard model: Group summary report, in GDR (Groupement De Recherche)—Supersymetrie, arXiv:hep-ph/9901246.

[32] P. Athron, M. Bach, D. Harries, T. Kwasnitza, J.-h. Park, D. Stöckinger, A. Voigt, and J. Ziebell, FlexibleSUSY 2.0: Extensions to investigate the phenomenology of SUSY and non-SUSY models, Comput. Phys. Commun. **230**, 145 (2018).

[33] P. Athron, J.-h. Park, D. Stöckinger, and A. Voigt, FlexibleSUSY—A spectrum generator generator for supersymmetric models, Comput. Phys. Commun. **190**, 139 (2015).

[34] B. C. Allanach, SOFTSUSY: A program for calculating supersymmetric spectra, Comput. Phys. Commun. **143**, 305 (2002).

[35] B. C. Allanach, P. Athron, L. C. Tunstall, A. Voigt, and A. G. Williams, Next-to-minimal SOFTSUSY, Comput. Phys. Commun. **185**, 2322 (2014).

[36] F. Staub, From superpotential to model files for FeynArts and CalcHep/CompHep, Comput. Phys. Commun. **181**, 1077 (2010).

[37] F. Staub, Automatic calculation of supersymmetric renormalization group equations and self energies, Comput. Phys. Commun. **182**, 808 (2011).

[38] F. Staub, SARAH 3.2: Dirac Gauginos, UFO output, and more, Comput. Phys. Commun. **184**, 1792 (2013).

[39] F. Staub, SARAH 4: A tool for (not only SUSY) model builders, Comput. Phys. Commun. **185**, 1773 (2014).

[40] P. Bambade *et al.*, The International Linear Collider: A Global Project, arXiv:1903.01629.

[41] A. Abada *et al.* (FCC Collaboration), FCC Physics Opportunities, Eur. Phys. J. C **79**, 474 (2019).

[42] A. Abada *et al.* (FCC Collaboration), FCC-ee: The Lepton Collider, Eur. Phys. J. Special Topics **228**, 261 (2019).

[43] H. Cheng, W. H. Chiu, Y. Fang, Y. Gao, J. Gu, G. Li *et al.*, The physics potential of the cepc. prepared for the us snowmass community planning exercise (snowmass 2021), arXiv:2205.08553.

[44] J. R. Andersen *et al.* (LHC Higgs Cross Section Working Group Collaboration), *Handbook of LHC Higgs Cross Sections: 3. Higgs Properties* (CERN, Geneva, 2013).

[45] P. Zyla *et al.* (Particle Data Group Collaboration), Review of Particle Physics, Prog. Theor. Exp. Phys. **2020**, 083C01 (2020).

[46] A. Djouadi, J. Kalinowski, and M. Spira, HDECAY: A Program for Higgs boson decays in the standard model and its supersymmetric extension, Comput. Phys. Commun. **108**, 56 (1998).

[47] M. Muhlleitner, A. Djouadi, and Y. Mambrini, SDECAY: A Fortran code for the decays of the supersymmetric particles in the MSSM, Comput. Phys. Commun. **168**, 46 (2005).

[48] A. Djouadi, M. M. Muhlleitner, and M. Spira, Decays of supersymmetric particles: The program SUSY-HIT (SUspect-SdecaY-Hdecay-InTerface), Acta Phys. Pol. B **38**, 635 (2007).

[49] P. Athron *et al.* (GAMBIT Models Workgroup Collaboration), SpecBit, DecayBit and PrecisionBit: GAMBIT modules for computing mass spectra, particle decay rates and precision observables, Eur. Phys. J. C **78**, 22 (2018).

[50] P. Athron, A. Büchner, D. Harries, W. Kotlarski, D. Stöckinger, and A. Voigt, FlexibleDecay: An automated calculator of scalar decay widths, arXiv:2106.05038.

[51] GAMBIT Collaboration, G. D. Martinez, J. McKay, B. Farmer, P. Scott, E. Roebber, A. Putze, and J. Conrad, Comparison of statistical sampling methods with ScannerBit, the GAMBIT scanning module, Eur. Phys. J. C **77**, 761 (2017).

[52] F. Feroz, M. P. Hobson, and M. Bridges, MultiNest: An efficient and robust Bayesian inference tool for cosmology and particle physics, Mon. Not. R. Astron. Soc. **398**, 1601 (2009).

[53] F. Feroz, M. P. Hobson, E. Cameron, and A. N. Pettitt, Importance nested sampling and the MultiNest algorithm, Open J. Astrophys. **2**, 10 (2019).

[54] N. Chen, T. Han, S. Su, W. Su, and Y. Wu, Type-II 2HDM under the Precision Measurements at the Z-pole and a Higgs Factory, J. High Energy Phys. 03 (2019) 023.

[55] M. Baak, J. Cúth, J. Haller, A. Hoecker, R. Kogler, K. Mönig, M. Schott, and J. Stelzer (Gfitter Group Collaboration), The global electroweak fit at NNLO and prospects for the LHC and ILC, Eur. Phys. J. C **74**, 3046 (2014).

[56] G. P. Lepage, P. B. Mackenzie, and M. E. Peskin, Expected precision of Higgs boson partial widths within the standard model, arXiv:1404.0319.

[57] J. Fan, M. Reece, and L.-T. Wang, Possible futures of electroweak precision: ILC, FCC-ee, and CEPC, J. High Energy Phys. 09 (2015) 196.

[58] M. Baak *et al.*, Working Group Report: Precision Study of Electroweak Interactions, in Community Summer Study 2013: Snowmass on the Mississippi, arXiv:1310.6708.

[59] P. Scott, Pippi—painless parsing, post-processing and plotting of posterior and likelihood samples, Eur. Phys. J. Plus **127**, 138 (2012).

[60] B. Abi *et al.* (Muon g-2 Collaboration), Measurement of the Positive Muon Anomalous Magnetic Moment to 0.46 ppm, Phys. Rev. Lett. **126**, 141801 (2021).

[61] P. Athron, C. Balázs, D. H. J. Jacob, W. Kotlarski, D. Stöckinger, and H. Stöckinger-Kim, New physics explanations of a_μ in light of the FNAL muon g-2 measurement, J. High Energy Phys. 09 (**2021**) 080.

[62] F. Wang, L. Wu, Y. Xiao, J. M. Yang, and Y. Zhang, GUT-scale constrained SUSY in light of new muon g-2 measurement, Nucl. Phys. **B970**, 115486 (2021).

[63] M. Endo, K. Hamaguchi, S. Iwamoto, and T. Kitahara, Supersymmetric interpretation of the muon g—2 anomaly, J. High Energy Phys. 07 (2021) 075.

[64] M. Abdughani, K.-I. Hikasa, L. Wu, J. M. Yang, and J. Zhao, Testing electroweak SUSY for muon $g - 2$ and dark matter at the LHC and beyond, J. High Energy Phys. 11 (2019) 095.

[65] J. Cao, F. Li, J. Lian, Y. Pan, and D. Zhang, Impact of LHC probes of SUSY and recent measurement of $(g-2)_\mu$ on $\mathbb{Z}_3$-NMSSM, arXiv:2204.04710.

[66] T. Aaltonen *et al.* (CDF Collaboration), High-precision measurement of the W boson mass with the CDF II detector, Science **376**, 170 (2022).

[67] E. Bagnaschi, M. Chakraborti, S. Heinemeyer, I. Saha, and G. Weiglein, Interdependence of the new "MUON G-2" Result and the W-Boson Mass, Eur. Phys. J. C **82**, 474 (2022).

[68] J. M. Yang and Y. Zhang, Low energy SUSY confronted with new measurements of W-boson mass and muon g-2, arXiv:2204.04202.

[69] P. Athron, M. Bach, D. H. J. Jacob, W. Kotlarski, D. Stöckinger, and A. Voigt, Precise calculation of the W boson pole mass beyond the Standard Model with FlexibleSUSY, arXiv:2204.05285.

[70] A. Djouadi, J.-L. Kneur, and G. Moultaka, SuSpect: A Fortran code for the supersymmetric and Higgs particle spectrum in the MSSM, Comput. Phys. Commun. **176,** 426 (2007).